HTO and Selenate Diffusion Through Compacted Na-, Na-Ca-, and Ca-Montmorillonite

Patricia M. Fox[a*], Christophe Tournassat[a,b], Carl Steefel[a], and Peter S. Nico[a]

[a] Earth and Environmental Sciences Area, Lawrence Berkeley National Laboratory, 1 Cyclotron Road, Berkeley, CA, USA

[b] ISTO, UMR 7327, Univ Orléans, CNRS, BRGM, OSUC, F-45071, France

*Corresponding author: pmfox@lbl.gov

Abstract

Radionuclide transport in smectite clay barrier systems used for nuclear waste disposal is controlled by diffusion, with adsorption significantly retarding transport rates. While a relatively minor component of spent nuclear fuel, ^{79}Se is a major driver of the safety case for spent fuel disposal due to its long half-life (3.3×10^5 yr) and its low adsorption to clay (K_D<10 L/kg), thus a thorough understanding of Se diffusion through clay is critical for understanding the long-term safety of spent fuel disposal systems. Through-diffusion experiments with tritiated water (HTO, conservative tracer) and Se(VI) were conducted with a well-characterized, purified montmorillonite source clay (SWy-2) under a constant ionic strength (0.1 M) and three different electrolyte compositions: Na^+, Ca^{2+}, and a Na^+-Ca^{2+} mixture at pH 6.5 in order to probe the effects of electrolyte composition and interlayer cation composition on clay microstructure, Se(VI) aqueous speciation, and ultimately diffusion. The results were modeled using a reactive transport modeling approach to determine values of porosity (ε), D_e (effective diffusion coefficient), and K_D (distribution coefficient for adsorption). HTO diffusive flux was higher in Ca-montmorillonite (D_e=1.68 × 10^{-10} m^2 s^{-1}) compared to Na-montmorillonite (D_e=7.83 × 10^{-11} m^2 s^{-1}). This increase in flux is likely due to a greater degree of clay layer stacking in the presence of Ca^{2+} compared to Na^+, which leads to larger inter-particle pores. Overall, the Se(VI) flux was much lower than the HTO flux due to anion exclusion, with Se(VI) flux following the order Ca (D_e=1.03 × 10^{-11} m^2 s^{-1})>Na-Ca (D_e=2.12 × 10^{-12} m^2 s^{-1})>Na (D_e=1.28 × 10^{-12} m^2 s^{-1}). These differences in Se(VI) flux are due to a combination of factors, including (1) larger accessible porosity in Ca-montmorillonite due to clay layer stacking and smaller electrostatic effects compared to Na-montmorillonite, (2) larger accessible porosity for neutral-charge CaSeO4 species which makes up 32% of aqueous Se(VI) in the pure Ca system, and (3) possibly higher Se(VI) adsorption for Ca-montmorillonite. Through a combination of experimental and modeling work, this study highlights the compounding effects that electrolyte and counterion compositions can have on radionuclide transport through clay. Diffusion models that neglect these effects are not transferable from laboratory experimental conditions to *in situ* repository conditions.

Keywords

Selenium diffusion; radioactive waste; interlayer cation; engineered barriers; anion exclusion

1. Introduction

Smectite clays, 2:1 layer-type phyllosilicate minerals, are the primary clay minerals found in bentonite and an important component of engineered barrier systems used for geologic storage of radioactive waste. Long-term nuclear waste disposal repositories must be capable of isolating radioactive waste over the time scales necessary for the decay of long-lived radioactive isotopes ($> 10^6$ years). Smectite clays are good barriers for radioactive waste due to their swelling capacity, ability to seal cracks, low hydraulic conductivity, and their high adsorption capacity for radionuclides. Montmorillonite is a common smectite mineral which has been widely studied. It has a large specific surface area (~750 m^2/g), cation exchange capacity (~1 mol_c/kg), and strongly-sorbing surface complexation sites on clay edge surfaces.

Natural smectites contain interlayer cations, including primarily Na^+, Ca^{2+}, and Mg^{2+}, which balance the negative permanent charge arising from isomorphic substitution in the phyllosilicate structure. The interlayer cation composition of smectite clays, including montmorillonite, affects the hydration and swelling properties of the clays (Bleam, 1990; Honorio et al., 2017; Laird and Shang, 1997; Salles et al., 2013; Subramanian and Nielsen Lammers, 2022; Teich-McGoldrick et al., 2015). For example, the presence of Na^+ in the interlayer leads to a higher degree of swelling compared to Ca^{2+} due to differences in the sizes and hydration energies of the cations. Natural smectites can have a wide range of interlayer cation compositions; Missana et al. (2018) studied bentonites currently under investigation for use in nuclear waste repositories and found Na^+ comprised <1 to 90% of the interlayer cation composition, with and Ca^{2+} and Mg^{2+} making up the bulk of the remainder. Groundwater intrusion into bentonite barriers can also alter the interlayer cation composition through cation exchange.

In compacted clay, solute transport is controlled by diffusion, and adsorption of solutes to the clay can significantly retard transport. While uranium is the primary constituent of radioactive waste, selenium (^{79}Se) is a major driver of the safety case for nuclear waste disposal due to its long half-life (3.3×10^5 yr) and presence as relatively mobile anionic species under a range of chemical conditions (*e.g.*, HSe^-, SeO_3^{2-}, SeO_4^{2-}). Se redox chemistry is complex, with oxidation states ranging from -II to +VI over environmentally relevant conditions. While Se(-II) and Se(0) are relatively immobile due to the formation of low solubility precipitates, Se(IV) and Se(VI) exist as the oxyanions selenite (SeO_3^{2-}) and selenate (SeO_4^{2-}) and are highly mobile in water due

to their high solubility. During deep geologic disposal of nuclear waste, the near field environment is characterized by a relatively short oxic period, followed by anoxic conditions. However, there is significant uncertainty and range in the Eh values expected, which will depend on numerous factors including the host rock type, bentonite composition, and waste canister corrosion. This makes it difficult to predict the speciation of Se in engineered barriers, however selenite and selenate are considered to be the dominant Se aqueous species released during oxidation of spent nuclear fuel (Ma et al, 2019; Chen et al., 1999). Se adsorption to clay minerals is quite low compared to other important radionuclides such as U. K_D values for selenite adsorption to smectite are in the range of 1-10 L/kg (Missana et al., 2009; Montavon et al., 2009) compared to values up to 10^4 for U(VI) (Tournassat et al., 2018). Selenite and selenate adsorption to the clay minerals kaolinite and Ca-montmorillonite were studied by Bar-Yosef and Meek (1987) over the pH range 4-8. Both selenite and selenate adsorption decreased with increasing pH, with very low or negligible adsorption above pH 8. Selenate adsorption to kaolinite was lower than selenite adsorption (Bar-Yosef and Meek, 1987).

Selenite diffusion through bentonite has been investigated in several studies (García-Gutiérrez et al., 2001; Idemitsu et al., 2016; Wang et al., 2016; Wu et al., 2017). Idemitsu et al. (2016) measured apparent diffusion coefficient (D_a) values of 2.5×10^{-11} to 1.9×10^{-13} m^2/s over a range of dry bulk densities (0.8-1.6 kg/L), ionic strengths (0.01-1.0 M NaCl), and temperatures (10-55°C) for purified bentonite consisting of 99% montmorillonite. Measured D_a values for bulk bentonite (*i.e.*, with lower smectite content) under similar conditions are 1-2 orders of magnitude higher (Sato et al., 1995; Wu et al., 2014). Due to the lower adsorption of selenate compared to selenite, selenate D_a values are expected to be even higher than observed for selenite, although we could find no studies on selenate diffusion through bentonite in the literature.

In this paper, we present experimental and modeling results from tritiated water (HTO) and Se(VI) through-diffusion experiments using a well-characterized, purified montmorillonite source clay (SWy-2) with different interlayer cation compositions (Na^+ and Ca^{2+}). Previous studies have observed higher diffusive flux of HTO (González Sánchez et al., 2008) and ReO_4^- (Wu et al., 2018) through Ca-montmorillonite compared to Na-montmorillonite. Selenate, with a charge of -2 and minimal adsorption, provides an opportunity to further probe anion diffusion (*i.e.*, for divalent species) in Na and Ca-montmorillonite systems and provide direct information

on ^{79}Se transport through clay barriers. Experiments were conducted under a single ionic strength (0.1 M) and three different electrolyte compositions representing pure Na^+, pure Ca^{2+}, and a Na^+-Ca^{2+} mixture in order to probe the effects of electrolyte composition and interlayer cation composition on clay microstructure, Se(VI) aqueous speciation, and ultimately diffusion.

2. Materials and Methods

2.1 Clay Samples

Selenium diffusion experiments were conducted using a well-characterized montmorillonite source clay (SWy-2) obtained from the Clay Minerals Society. The montmorillonite was purified in order to remove minor impurities (quartz, feldspars, and calcite). The purification procedure was adapted from Tinnacher et al. (2016). The procedure included the following major steps: (1) dialysis against sodium acetate at pH 5 for carbonate mineral dissolution, (2) dialysis against NaCl to remove acetate and complete Na-saturation, (3) dialysis against water to remove excess salts, and (4) centrifugation to remove quartz and feldspar particles greater than 2 μm. Montmorillonite (50 g) was suspended in 1 L of 1 M sodium acetate solution buffered at pH 5 with acetic acid, placed into pre-rinsed dialysis tubing (SpectraPor7, 8 kDa), and dialyzed against acetate buffer for 1 week, changing dialysis solution daily. The acetate buffer dialysis solution was then replaced with 1 M NaCl (dialyzed for 3 days), then with MilliQ water (dialyzed for two weeks), again changing dialysis solution daily. The clay suspensions were then transferred into plastic bottles and diluted and dispersed in MilliQ water to reach a clay concentration of approximately 15 g/L, and centrifuged at 1000 × *g* for 7 minutes. This centrifugation speed and time was deemed sufficient to remove all particles > 2 μm as calculated from Stoke's Law. The replicate < 2 μm clay fractions were then combined into a glass beaker, dried at 60°C and ground in ball mill with tungsten carbide balls.

In order to maintain constant aqueous porewater chemical conditions and interlayer cation composition during the diffusion experiments, purified montmorillonite was pre-equilibrated with the appropriate background electrolyte prior to packing in diffusion cells. 2 g of purified clay was suspended in 100 mL of electrolyte solution and the clay suspension was transferred to pre-rinsed dialysis tubing (SpectrPor7, 8 kDa). Clay samples were dialyzed against 1 L of background electrolyte for 1.5 weeks, changing dialysis solution at least 3 times and manually

adjusting pH daily. Once the pH remained between 6.45-6.55 within 24 hours, the background electrolyte solution was replaced with MilliQ water, and dialysis was continued for 5 days, changing the MilliQ water daily. After dialysis was complete, the clay suspension was transferred to 40 mL polycarbonate centrifuge tubes and centrifuged at 39 000 × *g* for 20 minutes. The supernatant was removed and the clay was dried at 60°C and ground in ball mill with tungsten carbide balls and stored at room temperature prior to packing the cells. At the time of packing, a subsample of each clay was dried at 150°C to determine the moisture content.

The cation exchange capacity (CEC) and exchangeable cation composition was measured using the hexamine cobalt(III) chloride method (Hadi et al., 2013). Triplicate samples of 50 mg dry clay were weighed into centrifuge tubes and 10 mL of 15 mM hexamine cobalt(III) chloride solution was added. Samples were mixed on an end-over-end sample rotator for 2 hours, then centrifuged at 39,000 x *g*. Solution samples were analyzed for major cations (Ca, Mg, K, and Na) by ICP-MS and the cation exchange capacity was calculated from the sum of cations released from the hexamine cobalt solution corrected for any soluble salts released during the water extracts. CEC is expressed as $mmol_c/g$ (mmol of charge per gram dry clay) and cation composition is expressed as the charge fraction for each cation.

2.2 Characterization of Filters

In order to accurately model diffusion through clay, the diffusion properties of the filters used in the diffusion cell must be explicitly considered. Therefore, diffusive properties of the filters were measured using custom-built filter diffusion cells based on a modified design of Aldaba et al. (2014). The cells consisted of two polycarbonate reservoirs with a filter connecting the two reservoirs. The filter is held in place with O-rings on each side and the two reservoirs are held together in a base plate. A one-hole silicone stopper was fitted in the top of each reservoir with a conductivity probe inserted through the hole to monitor solute diffusion. In addition, a small needle (22 G) was inserted through each stopper to allow venting and pressure equalization with the atmosphere. Without this venting needle, a small pressure differential can develop between the two cells due to slight differences in stopper insertion, causing water to flow between the two cells. Filters were made of PEEK with a PCTFE ring (IDEX # OC-815). The filters had an overall diameter of 0.95 cm, filter diameter of 0.74 cm, thickness of 0.16 cm, 5 µm pore size, and porosity of 0.26 according to the manufacturer.

The diffusion of sodium chloride was measured using this experimental setup in five replicate experiments. The filter was soaked in MilliQ water to remove air bubbles. 45 mL of MilliQ water was then added to each reservoir and allowed to equilibrate for at least 3 h. The low- and high-concentration reservoirs were then spiked with 5 mL MilliQ water or 1 M NaCl, respectively to start the experiment. This resulted in a concentration of 0.1 M NaCl in the high-concentration reservoir. Both reservoirs were stirred constantly throughout the experiment. The electrical conductivity of each reservoir was monitored with a conductivity probe and automatically logged every 30 min. The conductivity probes were calibrated with known concentrations of NaCl. During one experiment, 0.125 mL subsamples from each reservoir were collected and analyzed for Na by ICP-MS in order to verify that the conductivity measurements were accurately representing Na concentration. The measured Na concentrations agreed within 3% for the two methods.

2.3 Diffusion coefficient of filters

The cumulative mass (mol) of NaCl in the low-concentration reservoir was plotted over time (s). This results in a pseudo-linear breakthrough curve for the first ~100 h during which the concentration of NaCl in the high-concentration reservoir did not change significantly. The curve was fit with a linear regression and the effective diffusion coefficient (D_e) was determined using the slope (a) from the equation given by

$$D_e = \frac{a\,L}{A\,C_0} \qquad \text{Equation 1}$$

where L is the thickness of the filter, A is the cross-sectional area of the filter, and C_0 is the initial concentration in the high-concentration reservoir.

Effective diffusion coefficients measured for filters depend on the characteristics of both the filter and the solute, according to:

$$D_e = \frac{\varepsilon}{G} D_0 = \tau \varepsilon D_0 \qquad \text{Equation 2}$$

where D_0 is the bulk diffusion coefficient of a solute in water, while G (or $1/\tau$) is a geometric factor that accounts for the geometry of the filter pore network. τ is often referred to as the

tortuosity although it lumps together the true tortuosity and the constrictivity of the material. In this filter diffusion experiment D_0 refers to the co-diffusion of Na^+ and Cl^- (1.61×10^{-9} m^2s^{-1}), which is calculated from the diffusion coefficients of Na^+ and Cl^-, (1.33×10^{-9} and 2.03×10^{-9}, respectively at 25°C; Li and Gregory (1974) according to Cussler (2009) (see details in the SI). Diffusion coefficients of aqueous species were calculated using the filter parameters and the known D_0 values for those aqueous species. D_0 values at 25°C for HTO and SeO_4^{2-} were taken at 2.30×10^{-9} m^2 s^{-1} and 9.46×10^{-10} m^2 s^{-1} respectively.

2.4 Diffusion Experiments

Through-diffusion experiments were conducted with purified, pre-equilibrated montmorillonite at a dry bulk density (ρ_d) of approximately 1.3 kg L^{-1} corresponding to a total porosity (ε) of approximately 0.5 according to:

$$\varepsilon = 1 - \frac{\rho_d}{\rho_g} \qquad \text{Equation 3}$$

where ρ_g is the crystal density of clay mineral layers (*i.e.*, grain density). For montmorillonite, ρ_g is approximately 2.84 kg L^{-1} (Bourg et al., 2006; Tournassat and Appelo, 2011). The dry bulk density (ρ_d) is expressed in terms of the 150 °C oven dry weight of clay. There were some small differences in the calculated bulk density and porosity for the three diffusion cells because of differences in the moisture content of the clay at the time of packing (Table 2.).

The diffusion cells used for experiments are based on the design of (Van Loon et al., 2003), with dimensions adjusted to accommodate smaller samples (Figure S1). The clay plug inside the diffusion cells had a diameter of 9.5 mm and a length of 5 mm. Cells were machined in-house using PEEK (polyether ether ketone) plastic at Lawrence Berkeley National Laboratory.

Experiments were conducted under a single ionic strength (0.1 M) and three different electrolyte compositions: 0.1 M NaCl, 0.033 M $CaCl_2$, and 0.085 M NaCl + 0.005 M $CaCl_2$, representing pure Na^+, pure Ca^{2+}, and a Na^+-Ca^{2+} mixture, respectively. All experiments were performed at room temperature (23°C) at pH 6.5. The pre-equilibrated dry clay samples were weighed into PEEK diffusion cells and compacted using a custom PEEK packing rod.

The diffusion experiments were conducted in three phases: (1) saturation, (2) tritiated water (HTO) diffusion, and (3) Se(VI) diffusion. The clay was saturated by circulating 200 mL of background electrolyte at both ends of the cell at approximately 1 mL/min using a peristaltic pump for 40-42 days. After the saturation period, the HTO through-diffusion phase was started by replacing the background electrolyte solutions with a high HTO reservoir containing background electrolyte spiked with 1110 Bq mL^{-1} HTO (200 mL) at one end and a low HTO reservoir containing only background electrolyte (20 mL) at the other end. The high-concentration reservoir was sampled at the beginning and the end of the HTO diffusion experiment and did not change significantly over that time period. The low HTO reservoir was changed at time intervals of 3-36 h, and the HTO concentration was measured in the low reservoir samples by liquid scintillation counting. An in-house-built autosampler using a 3D printer (Creality Ender 3Pro) as the base was used to change the low reservoir samples at regular time intervals. The HTO concentration in the low reservoir never exceeded 0.5% of the concentration in the high reservoir. The HTO diffusion was continued for 16 days. After this period, the high-concentration reservoir was replaced with a Se(VI)-spiked solution containing 1.0 mM sodium selenate in the background electrolyte with a total volume of 190 mL, marking the start of the Se(VI) diffusion experiment. The low-concentration reservoirs containing only background electrolyte (5-10 mL) were changed at time intervals of 12-48 h for the first 44 days, then 48-170 h for the remaining 33 days, and Se concentrations were measured by ICP-MS. Se concentrations in the low reservoir never exceeded 1% of the concentration in the high reservoir. Subsamples of the high-concentration Se(VI) reservoir were collected at the beginning and end of the experiment and did not change significantly over the experiment.

At the end of the Se(VI) diffusion period, the diffusion cells were disassembled and the clay plug was extruded using the PEEK packing rod and sliced into thin slices. The thickness of the clay slices was measured using a digital caliper with a precision of 0.1 mm. Clay slices ranged in thickness from 0.3 to 0.9 mm. The clay slices were placed into 20 mL glass scintillation vials and dried at 150°C for 24 hours. The dried clay was extracted with 5 mL of 0.5 M trace metal grade hydrochloric acid for 3 days, then centrifuged at 39 000 × *g* for 20 min and filtered through a 0.45 μm PVDF syringe filter. Selenium concentrations were measured in the acid extracts by ICP-MS. Se concentrations in the clay profiles are expressed in mmol Se per liter of total porosity (C_{Se_pore}), calculated using the following equation:

$$C_{Se\_pore} = \frac{1000 \times C_{Se\_solid} \times \rho_d}{\varepsilon} \quad \text{Equation 4}$$

Where C_{Se_solid} is the concentration of Se extracted per gram of dry clay (in mmol g^{-1}).

2.5 Analytical Techniques

Samples were analyzed for Se by ICP-MS (Perkin-Elmer Elan DRC II) after acidification and dilution with ultrapure (ultrex grade) 0.15 M nitric acid and internal standard addition. Selenium was measured using oxygen as the cell gas in DRC mode and using Rh as an internal standard. Spike recoveries with known concentrations of Se were run every 5 samples, and recoveries ranged from 0.80-1.25. Independent QC samples were run every 10 samples, with recoveries ranging from 0.9-1.1. HTO samples were analyzed using liquid scintillation counting (Perkin-Elmer Liquid Scintillation Analyzer Tri-Carb 2900TR) by mixing 4 mL of sample with 18 mL of Ultima Gold XR liquid scintillation cocktail and counting until the relative standard deviation was 2% or for a maximum of 90 minutes.

2.6 Modeling Approach

Normalized mass flux (J_N, in m day^{-1}) reaching the low-concentration reservoir is most frequently calculated in the literature using:

$$J_N = \frac{C_{low} V_{low}}{C_{high} A \cdot \Delta t} \quad \text{Equation 5}$$

where C_{low} is the concentration in the low-concentration reservoir, C_{high} is the concentration in the high-concentration reservoir, V_{low} is the volume of the low-concentration reservoir (from ~5 to ~20 mL depending on the sampling event), A is the cross-sectional area of the diffusion cell (0.709 cm^2), and Δt is the time interval since the previous sampling event. This approximation is applicable for cases in which tracer concentration in the high reservoir does not change significantly over the course of the experiment (i.e., tracer source is considered infinite) and the tracer concentration in the low reservoir remains near zero (Yaroshchuk et al., 2008). However, for modeling purposes, this representation presents some problems (discussed in detail in Tournassat et al. (2023)), which include differences in time-integrated fluxes, J_N, compared to instantaneous fluxes calculated with the analytical solution of the diffusion equations. J_N values

may also oscillate with time because of the irregular pattern of sampling events during the experiment. A reactive transport modeling approach makes it possible to consider all experimental features such as the above-mentioned problems, as well as varying boundary conditions, the presence of filters, the presence of an O-ring in the filters, the replacement of the low-concentration reservoir with time, *etc.* (Tournassat et al., 2023). In addition, a reactive transport modeling approach allows comparison of the modeling results directly to the raw experimental data, *i.e.* the tracer concentrations measured in each of the collected vials at all sampling times. For these reasons, all clay sample diffusion experiments were modeled using the reactive transport model CrunchClay (Steefel and Tournassat, 2021; Tournassat and Steefel, 2021; Tournassat et al., 2020). The consideration of an O-ring in the filters necessitated carrying out the calculations with a 2D-axisymmetric geometry (Tournassat et al., 2023).

CrunchClay was used in combination with the CrunchEase interface (Tournassat et al., 2023) to estimate clay diffusive properties within the framework of a classical $\varepsilon - D_e - K_D$ modeling approach, where ε is the diffusion porosity (-), D_e is the effective diffusion coefficient ($m^2\ s^{-1}$, see Equation 2) and K_D ($L\ kg^{-1}$) is the distribution coefficient that accounts for reversible and linear adsorption processes. We assumed that HTO was present only in solution and that Se was present in solution (with c = aqueous concentration) and on surfaces (with C_{surf} in mol kg_{solid}^{-1}) so that C_{tot} (in mol m_{medium}^{-3}) can be expressed as:

$$C_{tot} = c\varepsilon + C_{surf}\rho_d \qquad \text{Equation 6}$$

We assumed that the Se surface concentration C_{surf} was linearly related to the aqueous concentration through $C_{surf} = cK_D$ (with K_D in $m^3_{water}\ kg_{solid}^{-1}$) and that the adsorption process was instantaneous and reversible. Based on this assumption,

$$C_{tot} = c\varepsilon + cK_D\rho_d. \qquad \text{Equation 7}$$

It was further assumed that the media were homogeneous. Hence D_e, ε, ρ_d and K_D are independent of x, and Fick's second law of diffusion reduces to:

$$\frac{\partial c}{\partial t} = \frac{\tau\varepsilon D_0}{\varepsilon + \rho_d K_D}\frac{\partial^2 c}{\partial x^2} = \frac{D_e}{\alpha}\frac{\partial^2 c}{\partial x^2} \qquad \text{Equation 8}$$

where α is the rock capacity factor.

The dimensions of the diffusion cells are available in the Supporting Information (Figure S1). The exact same dimensions were considered in our reactive transport simulations, which can be reproduced by the readers using the CrunchEase GUI made freely available on Github (https://github.com/Tournassat/CrunchEaseForAll).

In the following, the agreement of the model with the experimental data is shown on the raw data (concentration measurements in vials) and the experimental time-averaged flux J_N as a function of experimental conditions is only shown for comparison.

3. Results and Discussion

3.1 Filter Diffusion Properties

In order to characterize the baseline performance of the reaction cell, diffusion of NaCl through PEEK filters was measured in five replicate experiments. An example plot of cumulative NaCl mass in the low reservoir over time is shown in Figure S2. There was an initial lag period, followed by a linear increase in NaCl in the low reservoir. This linear portion of the breakthrough curve was used to calculate the effective diffusion coefficient of Na^+ and Cl^- through the filter according to Equation 1, resulting in a measured D_e of $6.1\times10^{-11} \pm 0.29\times10^{-11}$ $m^2\ s^{-1}$.

Given the known values for ε and D_0 (Table S1), we calculated G to be 6.82 ± 0.33 (τ = 0.147 ± 0.007). The measured D_e value was lower than for stainless steel filters with a similar pore size (1.6×10^{-10} $m^2\ s^{-1}$) (Aldaba et al., 2014). G and ε were slightly lower for the PEEK filters used in this experiment compared to those used by Aldaba et al. (2014), which had a smaller nominal pore size of 1 μm.

3.2 Clay Cation Composition

The total cation exchange capacity of the clay after purification was 0.833 ± 0.04 $mmol_c/g$. The cation composition for the Na, Na-Ca, and Ca exchanged clays is shown in Table 1. The cation composition is expressed as a % of charge (100×$mmol_c$ cation per gram/CEC in mmolc/g). The

Na-Ca clay contained 72% (by charge) Ca. A very small amount (1%) of exchangeable Mg was present in all three clays and no K was detected.

Table 1. Exchangeable cation composition of clays expressed as a charge % of the CEC.

Clay	Na (% charge)	Ca (% charge)	Mg (% charge)
Na	98.3 ± 0.6	0.5 ± 0.6	1.2 ± 0.0
Na-Ca	26.8 ± 0.2	72.2 ± 0.2	1.0 ± 0.0
Ca	1.6 ± 0.3	97.5 ± 0.2	0.9 ± 0.1

3.3 Tritiated water (HTO) diffusion

HTO diffusion reached a steady state after approximately 100 h, with steady-state fluxes increasing in the order Na, Na-Ca, and Ca (Figure 1). A precise estimation of the τ and D_e values of HTO was achieved by modeling the data with the assumption that the total porosity was accessible to HTO (Figure 1 and Table 2). The influence of the variations in sampling time intervals and sample vial volumes during the experiment is almost perfectly captured by our modeling approach (raw data available in the SI), thus giving confidence in the modeled τ and D_e values.

The small difference between the Na (τ_{HTO} = 0.065) and Na-Ca (τ_{HTO} = 0.070) cells might be attributed to small differences in cell packing (ρ_d = 1.35 vs. ρ_d =1.28 kg L^{-1} for Na and Na-Ca cells respectively). Differences in bulk density will affect not only the total porosity, but also the sample microstructure responsible for the geometrical factor affecting diffusion processes. Archie's law relates the effective diffusion coefficient to the porosity and an empirical cementation factor, *m*, that captures the change of the geometrical factor as a function of porosity changes:

$$D_e = D_0 \varepsilon^m \qquad \text{Equation 9}$$

Despite its empirical nature, Archie's law or its extended version (Van Loon and Mibus, 2015) is often able to quantitatively describe the evolution of the effective diffusion coefficient of HTO in clayey materials. The difference between the Na (τ_{HTO} = 0.065) and Na-Ca (τ_{HTO} = 0.070) cells

341 can be described by considering a cementation factor of $m \sim 3$, which is compatible with the
342 cementation factors commonly reported for bentonite samples (Van Loon and Mibus, 2015).
343 However, the difference between the Na-Ca ($\tau_{HTO} = 0.070$) and Ca ($\tau_{HTO} = 0.13$) cells cannot be
344 attributed to the small difference in cell packing only. A cementation factor of $m \sim 10$ would be
345 necessary, which does not fall in the range of values reported for montmorillonite. A reasonable
346 explanation of the observed difference lies in the difference of microstructure of Na- and Ca-
347 exchanged montmorillonite samples: the presence of exchangeable Ca promotes the formation of
348 thicker layer stacks ("tactoids") compared to Na (Segad et al., 2012), which in turn promotes the
349 presence of larger interparticle pores (Holmboe et al., 2012; Ohkubo et al., 2021), hence
350 increasing the diffusivity of the material (Melkior et al., 2009; Tournassat et al., 2011;
351 Tournassat et al., 2016).

352

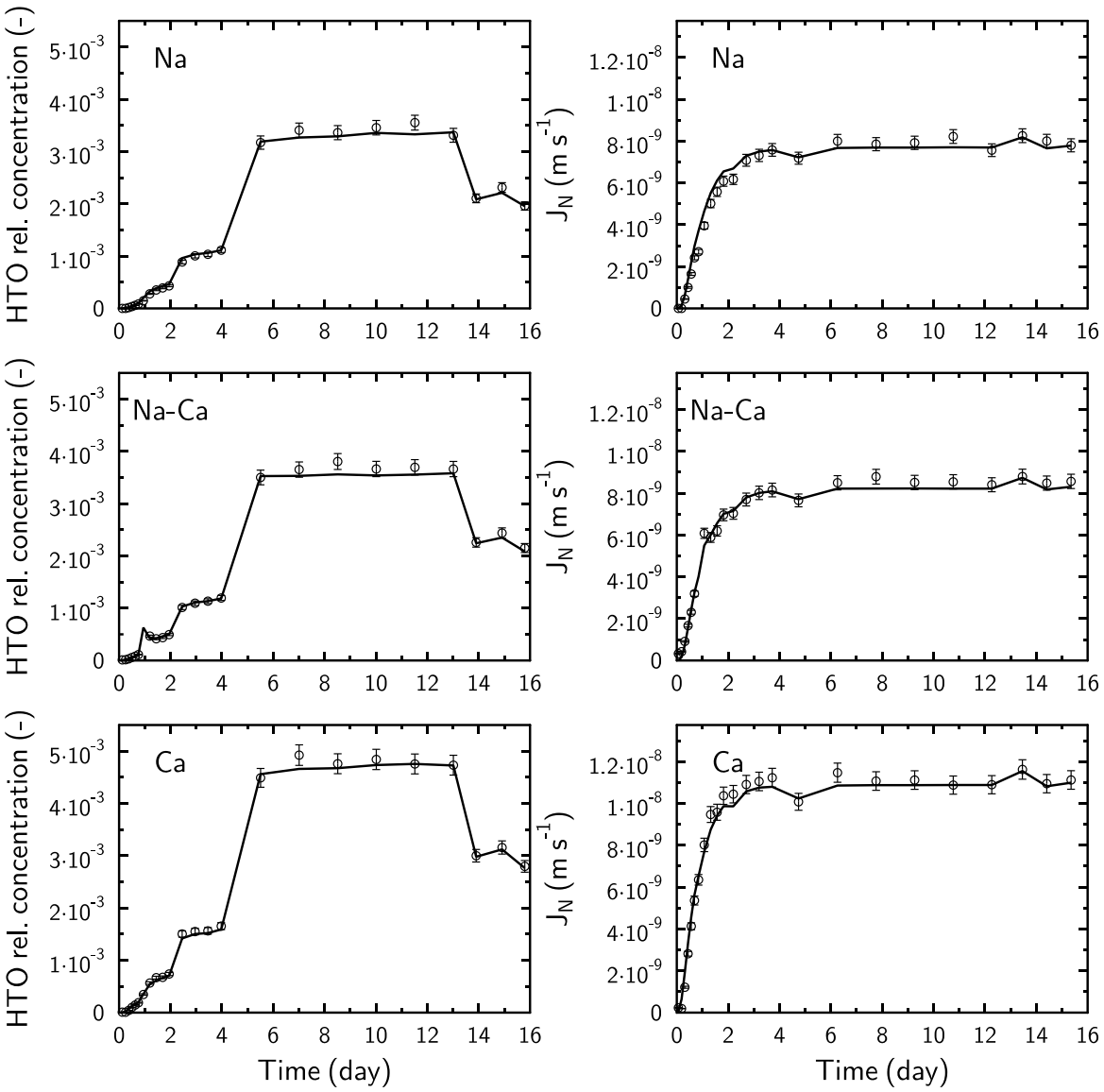

353

354 **Figure 1. Left: HTO normalized concentrations in the low-concentration reservoir as a**
355 **function of time. Right: HTO normalized flux as a function of time. Na, Na-Ca, and Ca**
356 **refers to the three different salt background and clay conditioning conditions. Circles:**
357 **experimental data; lines: results of the $\varepsilon - D_e$ models (Table *2.*). Error bars are**
358 **representative of the analytical error on the HTO measurements (2 standard deviations).**

359

360 **Table 2. Summary of measured diffusion cell parameters, including bulk density (ρ_d), total**
361 **porosity (ε_{tot}, calculated from Equation 3), along with reference model fitted parameters (τ,**

D_e, α_{Se}), assuming K_D = 0 L kg^{-1} for both HTO and Se(VI). Note that α_{HTO} is equivalent to ε_{HTO} and ε_{tot}. Uncertainties on the D_e value were estimated from model envelop curves and experimental error bars.

Cell	ρ_d (kg L^{-1})	$\varepsilon_{tot} = \varepsilon_{HTO} = \alpha_{HTO}$ (-)	τ_{HTO} (-)	$D_{e,HTO}$ (10^{-12} m^2 s^{-1})	$\alpha_{Se} = \varepsilon_{Se,max}$ (-)	$\tau_{Se,min}$ (-)	$D_{e,Se}$ (10^{-12} m^2 s^{-1})
Na	1.35	0.524	0.065	78 ± 4	0.0983	0.0138	1.3 ± 0.3
Na-Ca	1.28	0.551	0.070	89 ± 4	0.140	0.0160	2.1 ± 0.5
Ca	1.24	0.562	0.13	168 ± 8	0.450	0.0250	10.6 ± 2.3

3.4 Selenate diffusion

The normalized flux for Se(VI) reached steady state after approximately 300 h, with the Ca-montmorillonite showing the highest normalized flux (Figure 2). The steady-state flux of Se was much lower than that of HTO in all three cells. Total Se concentrations in clay slices also followed the trend Na<Na-Ca<Ca (Figure 3). Se concentrations in the clay slice closest to the high-concentration reservoir (at ~4.5-5.0 mm) were 0.18, 0.25, and 0.77 mM for the Na, Na-Ca, and Ca cells, respectively. The observed variations in Se concentration/flux may result from both differences in effective porosity for Se and from changes in Se adsorption in the presence of increasing Ca concentrations. The profiles in all three cells were linear with depth as expected for steady-state conditions.

Through-diffusion data makes it possible to extract a single set of α, D_e values for each tracer in one experiment (Crank, 1975; Van Loon et al., 2003). However, it does not provide enough constraints to extract a single set of ε, K_D, and τ values and additional data and/or hypotheses are necessary to derive these three quantities independently. In the first attempt, the K_D values for Se(VI) were set to zero. In this condition, the fitted porosity and tortuosity values take their maximum and minimum value respectively ($\varepsilon_{max} = \alpha$ and τ_{min}; Table 2). The corresponding fitted parameters made it possible to almost perfectly reproduce the diffusion data (Figure 2 and Figure 3).

In Na-montmorillonite, clay layers are negatively charged and part or all of the porosity is influenced by the presence of an electrical double layer (EDL) that forms at the surface, and in which the solution is not electroneutral (Tournassat and Steefel, 2019). Negatively charged species, including SeO_4^{2-}, are depleted in the EDL-influenced portion of the porosity because of their interaction with the negative electrostatic potential field created by the surfaces of montmorillonite. This process, often called anion-exclusion, is also responsible for a higher geometrical factor, G (or $1/\tau$), for anions compared to neutral tracers such as HTO, because pore throats, which are responsible for the pore network connectivity, may partially or totally exclude anions, thus ascribing longer diffusion pathways to anions compared to neutral species. Consequently, $\tau_{Se} \leq \tau_{HTO}$ and it is possible to define a minimum accessible porosity value for Se corresponding to $D_{e,Se} = \tau_{HTO} \times \varepsilon_{Se,min} \times D_{0,Se}$. This minimum porosity corresponds itself to a maximum K_D value according to $\alpha_{Se} = \varepsilon_{Se,min} + \rho_d K_{D,max}$ (Table 3). We note that the very low $K_{D,max}$ values (<<1) in Table 3 are nearly impossible to measure in batch experiments.

The calculated minimum value of SeO_4^{2-} accessible porosity ($\varepsilon_{Se,min} = 0.021$) was similar to the values reported for Cl^- in similar compacted Na-montmorillonite materials (Tournassat and Appelo, 2011). Cl^- does not adsorb on clay mineral surfaces, and thus, the difference between total porosity values and Cl^- accessible porosity values reported in the literature are truly representative of the excluded volume for monovalent anions. However, one would expect an increased exclusion for SeO_4^{2-} compared to Cl^- because of their difference in charge. This surprisingly high Se(VI) accessible porosity in the Na-montmorillonite sample may be partly explained by the presence of aqueous and exchanged Mg^{2+} which originates from a limited dissolution of the clay layers (Orucoglu et al., 2018). The formation of $MgSeO_4$ ion pairs, which are neutral and, thus not excluded from the EDL, would then explain the lower value of Se(VI) exclusion than expected. Mg^{2+} was a minor component (1%) of exchangeable cations at the beginning of the experiment (Table 1). However, we did not measure exchangeable cations on the clay at the end of the experiment or aqueous Mg^{2+} during the diffusion experiment, therefore are unable to confirm the formation of $MgSeO_4$ ion pairs. The lowering of Se exclusion from the EDL could also be related to an increased ion pairing in the EDL compared to bulk water conditions (Appelo et al., 2010), which in turn would increase the apparent accessible porosity of Se.

Table 3. Summary of constraints on Se diffusion parameters in Na-, Na-Ca-, and Ca-montmorillonite. $K_{D,max}$ values are given in L kg^{-1}.

Cell	$\varepsilon_{Se,min}$	$K_{D,max}$	$\varepsilon_{Se,min}$ considering $CaSeO_4$ ion pair formation	$K_{D,max}$ considering $CaSeO_4$ ion pair formation
Na	0.021	0.057	-	-
Na-Ca	0.032	0.084	0.036	0.081
Ca	0.086	0.29	0.18	0.22

In the Ca-montmorillonite sample, the minimum accessible porosity was found to be 0.086. This higher accessible porosity for Ca-montmorillonite compared to the Na-montmorillonite sample can be explained by a combination of the following effects: the presence of wider interparticular pores, which increases the average anion accessible porosity (Tournassat et al. 2016) and a decrease of the magnitude of the negative electrostatic potential field in the presence of divalent cations (Ca^{2+}). However, the presence of $CaSeO_4$ aqueous complexes which are neutral and thus not repelled from clay mineral surfaces will also affect the minimum accessible porosity, which is not accounted for in the above estimate ($\varepsilon_{Se,min}$ of 0.086 for Ca). Aqueous speciation calculation carried out with the Thermochimie database (Giffaut et al., 2014; https://www.thermochimie-tdb.com/) indicates that 32% of the total Se concentration is present in the form of $CaSeO_4$ in a 0.033 M $CaCl_2$ background solution. Equivalently, at least 32% of the total porosity is accessible to Se in this neutral form, *i.e.* a revised minimum accessible porosity of $0.32 \times 0.56 = 0.18$, giving in turn a revised $K_{D,max}$ value of 0.22 L kg^{-1} (Table 3.). Assuming that the D_0 value for $CaSeO_4$ is similar to that of $CaSO_4$ ($D_0 = 4.71\ 10^{-10}$ m^2 s^{-1} available from the PHREEQC.dat database), a $\tau_{Se,max}$ value of 0.115 can be deduced.

In the Na-Ca cell, with 0.005 M $CaCl_2$ + 0.085 M NaCl background solution, 6.6% of the total aqueous Se(VI) is in the form of $CaSeO_4$, leading to a minimum accessible porosity of $\varepsilon_{Se,min} = 0.066 \times 0.55 = 0.036$. The corresponding $\tau_{Se,max}$ value is 0.123, which is very similar to the value found for the Ca-montmorillonite sample.

437 The above analysis highlights the importance of a good knowledge of the aqueous speciation to
438 understand and predict the diffusion properties of Se and provides realistic constraints for the
439 ranges of ε_{Se}, K_{DSe}, and τ_{Se}.

440

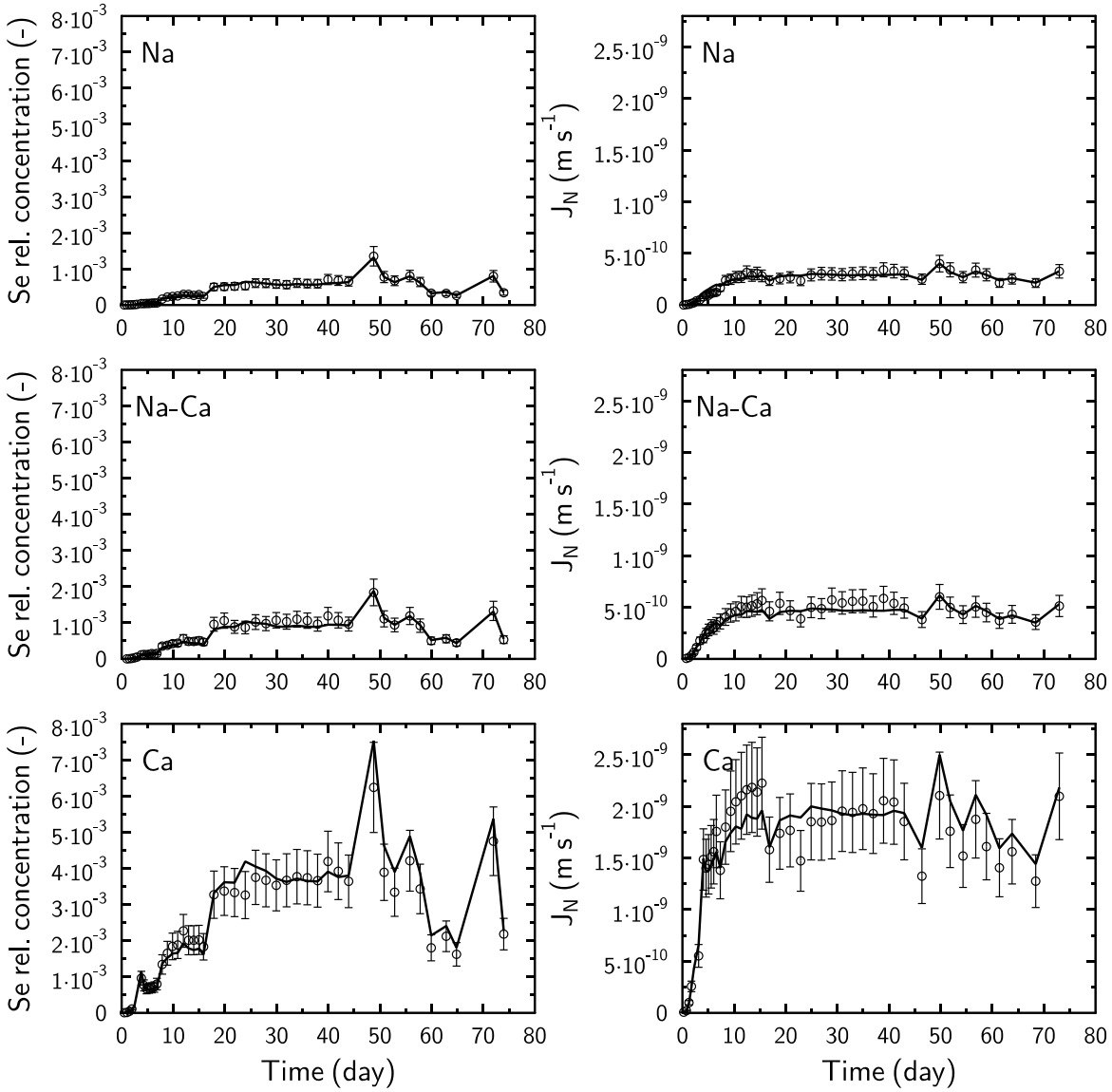

441

442 **Figure 2. Left: Se normalized concentrations in the low-concentration reservoir as a**
443 **function of time. Right: Se normalized flux as a function of time. Na, Na-Ca, and Ca refers**
444 **to the three different salt background and clay conditioning conditions. Circles:**
445 **experimental data; lines: results of the ε – D_e – K_D models (Table 2.) where K_D is assumed**

to be 0. Error bars are representative of the analytical error on the Se measurements. The y-axis scale is the same for all conditions to ease a direct comparison.

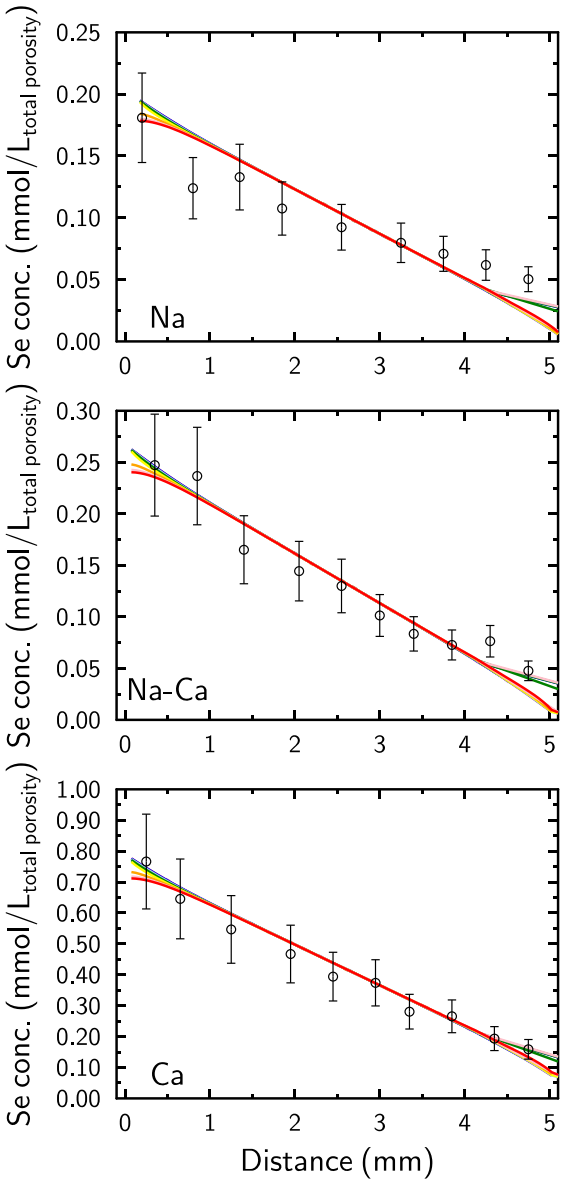

Figure 3. Total Se profiles in clay at the end of diffusion experiments. Se concentrations are expressed as a concentration in the total porewater volume. Circles: experimental data; lines: simulated profiles using the same α_{Se} and $D_{e,Se}$ as in Figure 2. The different colors are

indicative of the different profile positions in the radial direction (the red color is for the central grid-cells on the symmetry axis). Error bars represent the analytical error (2 standard deviations). Note that the concentrations at the downstream boundary do not tend to zero because of the O-ring and the presence of tubings (i.e., 'dead volumes') in which the tracers are accumulating between sampling events.

4. Conclusions

An increase of Ca/Na ratio in solution and on clay surfaces is responsible for an increase in HTO and selenate diffusivity in montmorillonite samples. The increase of HTO diffusivity can be explained by a change of microstructure leading to an increase of the τ_{HTO} value. These changes will affect the transport of all radionuclides through clay barriers, including Se. In addition, the aqueous speciation of Se(VI) has a large effect on Se transport. Se(VI) diffusion is limited by anion exclusion due to the formation of the negatively charged species SeO_4^{2-}. However, in the presence of Ca^{2+}, the formation of $CaSeO_4$ neutral ion pairs, which can access a larger portion of the total porosity, increases selenate diffusivity. While additional insights about the exact distribution of the interlayer and interparticle porosities and the influence of the diffuse layer on selenate ion pair formation would be necessary to build a comprehensive mechanistic model for selenate diffusion in montmorillonite samples, we provide constraints on model parameters that can be used to predict a range of Se(VI) transport in engineered barrier systems. Our analysis highlights that Se(VI) diffusion parameters (*e.g.*, effective diffusion coefficients) obtained with simplified laboratory systems cannot be transferred to the simulation of a repository if *in situ* geochemical conditions, especially ionic strength and major element concentrations (*e.g.*, Ca), are different from the laboratory conditions. Furthermore, these results have similarly important implications for the diffusion of other radionuclides which are present as anions or mixed-species in waste repositories, including Se(IV) ($HSeO_3^-$, SeO_3^{2-}), U(VI) (e.g., $UO_2(OH)_3^-$, $UO_2(OH)_4^{2-}$), Mo(VI) (MoO_4^{2-}) and others. Radionuclide aqueous speciation together with the presence of an EDL must be explicitly taken into account in the model in order to accurately predict their transport. The results also emphasize the need to understand the overall chemical evolution of repository conditions as changes in aqueous speciation due to many factors (*e.g.*,

mineral dissolution/precipitation or groundwater penetration) can change the mobility of important species.

Supplementary Material

Supplementary information, including diffusion cell schematics and additional information about measuring diffusive properties of the filters is provided in a separate file and is available free of charge online.

Data Availability

Raw experimental data used in this manuscript is available on Mendeley Data (Fox et al., 2024).

Acknowledgements

This work was supported by the Spent Fuel and Waste Science and Technology Program, Office of Nuclear Energy of the US Department of Energy under contract number DE-AC02-05CH11231 with Lawrence Berkeley National Laboratory.

References

Aldaba, D., Glaus, M., Leupin, O., Loon, L.V., Vidal, M., Rigol, A., 2014. Suitability of various materials for porous filters in diffusion experiments. Radiochimica Acta 102, 723-730.

Appelo, C., Van Loon, L., Wersin, P., 2010. Multicomponent diffusion of a suite of tracers (HTO, Cl, Br, I, Na, Sr, Cs) in a single sample of Opalinus Clay. Geochimica et Cosmochimica Acta 74, 1201-1219.

Bar-Yosef, B., Meek, D., 1987. Selenium Sorption by Kaolinite and Montmorillonite. Soil Science 144, 11-19.

Bleam, W.F., 1990. The Nature of Cation-Substitution Sites in Phyllosilicates. Clays and Clay Minerals 38, 527-536.

Bourg, I.C., Sposito, G., Bourg, A.C.M., 2006. Tracer diffusion in compacted, water-saturated bentonite. Clays and Clay Minerals 54, 363-374.

507 Chen, F., Burns, P.C., Ewing, R.C., 1999. 79Se: geochemical and crystallo-chemical retardation
508 mechanisms. Journal of Nuclear Materials 275, 81-94.

509 Crank, J., 1975. The mathematics of diffusion. Oxford University Press.

510 Cussler, E. L., 2009. Diffusion: mass transfer in fluid systems, Cambridge university press.García-
511 Gutiérrez, M., Missana, T., Mingarro, M., Samper, J., Dai, Z., Molinero, J., 2001. Solute transport
512 properties of compacted Ca-bentonite used in FEBEX project. Journal of Contaminant Hydrology
513 47, 127-137.

514 Giffaut, E., Grivé, M., Blanc, P., Vieillard, P., Colàs, E., Gailhanou, H., Gaboreau, S., Marty, N.,
515 Madé, B., Duro, L., 2014. Andra thermodynamic database for performance assessment:
516 ThermoChimie. Applied Geochemistry 49, 225-236.

517 Fox, P. M., Tournassat, C., Steefel, C., Nico, P.S., 2024. Data for: HTO and Selenate Diffusion
518 Through Compacted Na-, Na-Ca-, and Ca-Montmorillonite. Mendeley Data. DOI:
519 10.17632/9wy2v6tpxk.1

520 González Sánchez, F., Van Loon, L.R., Gimmi, T., Jakob, A., Glaus, M.A., Diamond, L.W., 2008.
521 Self-diffusion of water and its dependence on temperature and ionic strength in highly compacted
522 montmorillonite, illite and kaolinite. Applied Geochemistry 23, 3840-3851.

523 Hadi, J., Tournassat, C., Ignatiadis, I., Greneche, J.M., Charlet, L., 2013. Modelling CEC
524 variations versus structural iron reduction levels in dioctahedral smectites. Existing approaches,
525 new data and model refinements. J.Colloid Interface Sci. 407, 397-409. DOI:
526 10.1016/j.jcis.2013.05.014

527 Holmboe, M., Wold, S., Jonsson, M., 2012. Porosity investigation of compacted bentonite using
528 XRD profile modeling. Journal of Contaminant Hydrology 128, 19-32.

529 Honorio, T., Brochard, L., Vandamme, M., 2017. Hydration Phase Diagram of Clay Particles from
530 Molecular Simulations. Langmuir 33, 12766-12776.

531 Idemitsu, K., Kozaki, H., Yuhara, M., Arima, T., Inagaki, Y., 2016. Diffusion behavior of selenite
532 in purified bentonite. Progress in Nuclear Energy 92, 279-285.

Laird, D.A., Shang, C., 1997. Relationship Between Cation Exchange Selectivity and Crystalline Swelling in Expanding 2:1 Phyllosilicates. Clays and Clay Minerals 45, 681-689.

Li, Y.-H., Gregory, S., 1974. Diffusion of ions in sea water and in deep-sea sediments. Geochimica et Cosmochimica Acta 38, 703-714.

Ma, B., Charlet, L., Fernandez-Martinez, A., Kang, M., Madé, B., 2019. A review of the retention mechanisms of redox-sensitive radionuclides in multi-barrier systems. Applied Geochemistry 100, 414-431.

Melkior, T., Gaucher, E.C., Brouard, C., Yahiaoui, S., Thoby, D., Clinard, C., Ferrage, E., Guyonnet, D., Tournassat, C., Coelho, D., 2009. Na+ and HTO diffusion in compacted bentonite: Effect of surface chemistry and related texture. Journal of Hydrology 370, 9-20.

Missana, T., Alonso, U., Fernández, A.M., García-Gutiérrez, M., 2018. Colloidal properties of different smectite clays: Significance for the bentonite barrier erosion and radionuclide transport in radioactive waste repositories. Applied Geochemistry 97, 157-166.

Missana, T., Alonso, U., García-Gutiérrez, M., 2009. Experimental study and modelling of selenite sorption onto illite and smectite clays. Journal of Colloid and Interface Science 334, 132-138.

Montavon, G., Guo, Z., Lützenkirchen, J., Alhajji, E., Kedziorek, M.A.M., Bourg, A.C.M., Grambow, B., 2009. Interaction of selenite with MX-80 bentonite: Effect of minor phases, pH, selenite loading, solution composition and compaction. Colloids and Surfaces A: Physicochemical and Engineering Aspects 332, 71-77.

Ohkubo, T., Yamazaki, A., Fukatsu, Y., Taichi, Y., 2021. Pore distribution of compacted Ca-montmorillonite using NMR relaxometry and cryoporometry: Comparison with Na-montmorillonite. Microporous and Mesoporous Materials 313, 110841.

Orucoglu, E., Tournassat, C., Robinet, J.-C., Made, B., Lundy, M., 2018. From experimental variability to the sorption related retention parameters necessary for performance assessment models for nuclear waste disposal systems: The example of Pb adsorption on clay minerals. Applied Clay Science 163, 20-32.

559 Salles, F., Douillard, J.-M., Bildstein, O., Gaudin, C., Prelot, B., Zajac, J., Van Damme, H., 2013.
560 Driving force for the hydration of the swelling clays: Case of montmorillonites saturated with
561 alkaline-earth cations. Journal of Colloid and Interface Science 395, 269-276.

562 Segad, M., Hanski, S., Olsson, U., Ruokolainen, J., Åkesson, T., Jönsson, B., 2012.
563 Microstructural and Swelling Properties of Ca and Na Montmorillonite: (In Situ) Observations
564 with Cryo-TEM and SAXS. The Journal of Physical Chemistry C 116, 7596-7601.

565 Steefel, C.I., Tournassat, C., 2021. A model for discrete fracture-clay rock interaction
566 incorporating electrostatic effects on transport. Computational Geosciences 25, 395-410.

567 Subramanian, N., Nielsen Lammers, L., 2022. Thermodynamics of ion exchange coupled with
568 swelling reactions in hydrated clay minerals. Journal of Colloid and Interface Science 608, 692-
569 701.

570 Teich-McGoldrick, S.L., Greathouse, J.A., Jové-Colón, C.F., Cygan, R.T., 2015. Swelling
571 Properties of Montmorillonite and Beidellite Clay Minerals from Molecular Simulation:
572 Comparison of Temperature, Interlayer Cation, and Charge Location Effects. The Journal of
573 Physical Chemistry C 119, 20880-20891.

574 Tinnacher, R.M., Holmboe, M., Tournassat, C., Bourg, I.C., Davis, J.A., 2016. Ion adsorption and
575 diffusion in smectite: Molecular, pore, and continuum scale views. Geochimica et Cosmochimica
576 Acta 177, 130-149.

577 Tournassat, C., Appelo, C.A.J., 2011. Modelling approaches for anion-exclusion in compacted Na-
578 bentonite. Geochimica et Cosmochimica Acta 75, 3698-3710.

579 Tournassat, C., Bizi, M., Braibant, G., Crouzet, C., 2011. Influence of montmorillonite tactoid size
580 on Na–Ca cation exchange reactions. Journal of Colloid and Interface Science 364, 443-454.

581 Tournassat, C., Gaboreau, S., Robinet, J.-C., Bourg, I.C., Steefel, C.I., 2016. Impact of
582 microstructure on anion exclusion in compacted clay media.

583 Tournassat, C., Steefel, C.I., 2021. Modeling diffusion processes in the presence of a diffuse layer
584 at charged mineral surfaces: a benchmark exercise. Computational Geosciences 25, 1319-1336.

585 Tournassat, C., Steefel, C.I., Fox, P.M., Tinnacher, R.M., 2023. Resolving experimental biases in
586 the interpretation of diffusion experiments with a user-friendly numerical reactive transport
587 approach. Scientific Reports 13, 15029.

588 Tournassat, C., Steefel, C.I., Gimmi, T., 2020. Solving the Nernst-Planck equation in
589 heterogeneous porous media with finite volume methods: Averaging approaches at interfaces.
590 Water resources research 56, e2019WR026832.

591 Tournassat, C., Tinnacher, R.M., Grangeon, S., Davis, J.A., 2018. Modeling uranium(VI)
592 adsorption onto montmorillonite under varying carbonate concentrations: A surface complexation
593 model accounting for the spillover effect on surface potential. Geochimica et Cosmochimica Acta
594 220, 291-308.

595 Van Loon, L.R., Mibus, J., 2015. A modified version of Archie's law to estimate effective
596 diffusion coefficients of radionuclides in argillaceous rocks and its application in safety analysis
597 studies. Applied Geochemistry 59, 85-94.

598 Van Loon, L.R., Soler, J.M., Bradbury, M.H., 2003. Diffusion of HTO, 36Cl− and 125I− in
599 Opalinus Clay samples from Mont Terri: Effect of confining pressure. Journal of Contaminant
600 Hydrology 61, 73-83.

601 Wang, Z., Wang, H., Li, Q., Xu, M., Guo, Y., Li, J., Wu, T., 2016. pH effect on Re(VII) and Se(IV)
602 diffusion in compacted GMZ bentonite. Applied Geochemistry 73, 1-7.

603 Wu, T., Wang, Z., Wang, H., Zhang, Z., Van Loon, L.R., 2017. Salt effects on Re(VII) and Se(IV)
604 diffusion in bentonite. Applied Clay Science 141, 104-110.

605 Wu, T., Wang, Z., Tong, Y., Want, Y., Van Loon, L.R., 2018. Investigation of Re(VII) diffusion
606 in bentonite by through-diffusion and modeling techniques. Applied Clay Science 166, 223-229.

607 Yaroshchuk, A. E., Glaus, M., Van Loon, L.R., 2008. Diffusion through confined media at variable
608 concentrations in reservoirs. Journal of Membrane Science 319(1): 133-140.

609